A Generalized Method for Optimizing Impedance Matching in Capacitively Coupled Plasmas

Dehen Cao,[1] Shimin Yu,[2] Hongyu Wang,[3] Zhipeng Chen,[2] Wei Jiang,[1, 2] and Ya Zhang[4]
[1)]*School of Physics, Huazhong University of Science and Technology, Wuhan 430074, China*
[2)]*International Joint Research Laboratory of Magnetic Confinement Fusion and Plasma Physics, State Key Laboratory of Advanced Electromagnetic Engineering and Technology, School of Electrical and Electronic Engineering, Huazhong University of Science and Technology, Wuhan 430074, China*
[3)]*School of Physics Science and Technology, Anshan Normal University, Anshan 114000, China*
[4)]*Department of Physics, Wuhan University of Technology, Wuhan 430070, China*

(*Electronic mail: yazhang@whut.edu.cn)

(*Electronic mail: weijiang@hust.edu.cn)

(Dated: 19 July 2026)

Impedance matching in capacitively coupled plasma (CCP) systems is crucial. However, due to the complex nonlinear interactions between the plasma and the external circuit, identifying control parameters that enable efficient and robust power transfer remains particularly challenging. Traditional optimization methods, rely on favorable initial conditions for convergence. Even when successful, they yield only a single set of control parameters and often require highly complex optimization designs due to strong coupling with the CCP load. To address these challenges, we propose a simpler yet more robust optimization method by shifting the optimization process from the control parameter space to the load's complex impedance space. In this approach, the load impedance acts as a bridge between the new and old control parameters, decoupling the derivation of new parameters from historical trajectories. This eliminates dependence on initial conditions and enables the method to yield multiple sets of control parameters at different saddle positions. Additionally, the load impedance also acts as a bridge between the optimization algorithm and the load device, decoupling complex physical details from the optimization process, making our method remain consistent across both numerical simulations and experimental setups. In this paper, when applying the method to a numerical CCP system with an L-type matching network, it not only achieved efficient energy matching optimization within a few iterations but also identified multiple well-matched solutions.

I. INTRODUCTION

Impedance matching is essential for capacitively coupled plasma (CCP) systems, which are widely used in various industrial applications, such as semiconductor manufacturing, surface modification, and thin film deposition[1–5]. The primary goal of impedance matching is to achieve optimal energy coupling between the power source and the plasma load, ensuring better process control, improved plasma uniformity, and minimized energy loss[6,7].

Researchers and engineers have developed various techniques to achieve efficient matching in plasma systems. Traditional methods often use adjustable capacitor-inductor networks, such as L-type[8,9], π-type[10], or T-type[11] configurations, to manually or automatically tune the load impedance to match the source impedance. Alternatively, impedance matching can also be accomplished by adjusting the driving frequency or power supply waveform[12–16]. In experiments, Parro et al.[17] developed an automatic impedance matching system using gradient-based algorithms and adjustable mechanical posts to minimize reflection coefficients in industrial microwave ovens. Franek et al.[18] implemented an impedance matching network (IMN) that customizes voltage waveforms and independently controls harmonics to optimize ion energy distribution. Wang et al.[19] demonstrated a multi-frequency matching technique with an LC resonant circuit matchbox, successfully achieving simultaneous harmonic matching for surface processing. Khomenko et al.[20] explored CCP discharges as tunable impedance elements, showing that plasma excitation frequency and power can control impedance properties. Missen et al.[21] developed a plasma-switch impedance tuner using gas discharge tubes for rapid switching, enabling wideband tuning in dynamic RF environments.

For numerical methods, Li et al.[6] analyzed transmission line effects in RF microplasma discharge, demonstrating that adjusting line length and capacitance can optimize matching and regulate high terminal voltages. Schmidt et al.[22] integrated a nonlinear equivalent circuit plasma model with an L-type matching network, solving Kirchhoff's equations and iteratively adjusting plasma parameters to achieve optimal matching. Yu et al.[23] performed iterative simulations to optimize control parameters, significantly reducing reflection coefficients and improving power absorption efficiency. In follow-up research, Yu further explored transmission line model-based matching[24]. Tian et al.[25] employed 2D particle in cell / Monte Carlo collision (PIC/MCC) simulations to investigate the uniformity in dual-frequency CCP at 1.356 MHz and 27.12 MHz, identifying how pressure and voltage influence plasma profiles and ion energy distributions. Cao et al.[26] applied an artificial neural network (ANN) as a surrogate model for CCP matching optimization, enhancing the efficiency of saddle points exploration. Yuan et al.[27] studied a 13.56 MHz CCP with various π-type matching networks using a MATLAB-based nonlinear global model and FFT analysis, demonstrating that a specific configuration effectively suppresses higher-order harmonics and improves plasma symmetry.

However, the aforementioned methods either struggle to converge, converge only to a single local optimum, or involve highly time-consuming processes. Moreover, many of these methods are closely tied to specific devices, limiting their adaptability to varying discharge conditions. As a result, a universal and robust optimization method for CCP impedance matching has yet to be developed. In fact, the key limitation of existing methods lies in their forward-adjustment strategies, where each set of control parameters is directly derived from the previous one, creating a strong dependence on the past iterations. This not only makes the choice of initial conditions crucial but also makes it difficult for the system to escape saddle points. To address this, we propose a novel matching strategy based on inverse reasoning. By shifting the optimization process from the control parameter space to the plasma impedance space, new control parameters are inversely derived from the impedance space. The plasma impedance serves as a bridge between the old and new control parameters, decoupling them from their historical trajectories. The resulting path-independent nature enables optimization from any initial state, removing the dependence on favorable initial conditions and significantly enhancing robustness. Furthermore, the plasma impedance, being a measurable parameter, effectively conceals the internal modeling details of the plasma, making this optimization method applicable to 1D, 2D, and 3D simulations, as well as practical applications. Additionally, the path-independent characteristic of our method inherently allows for the exploration of multiple saddle points, enabling a comprehensive gathering of well-matched point distributions, thereby offering more optimization possibilities. This feature sets our method apart from conventional approaches.

This paper is organized as follows: Sec. II introduces the optimization strategy and the relevant modeling methods. Sec. III provides a detailed example of the method's implementation and discusses how each component influences the optimization results. Finally, Sec. IV summarizes the conclusions.

II. METHOD

Fig. 1 shows the workflow of our optimization method, which aims to find the optimal control parameter set P by minimizing the objective parameter λ. The workflow includes the following steps:

Step 1: Coupled circuit model construction.

To clarify the optimization process, we designed a streamlined coupling circuit, shown in Fig. 2, as a case study for optimization. From left to right, the circuit can be divided into three parts: (i) An RF source with a fixed internal resistance R_s. The source operates at a single, fixed frequency f_s, and delivers a steady output power P_s. The voltage drop across the source is denoted as U_s. (ii) An L-type matching network, consisting of two variable capacitors C_{m1} and C_{m2}, a variable inductor L, and a fixed resistor R_m. R_m is used to calculate

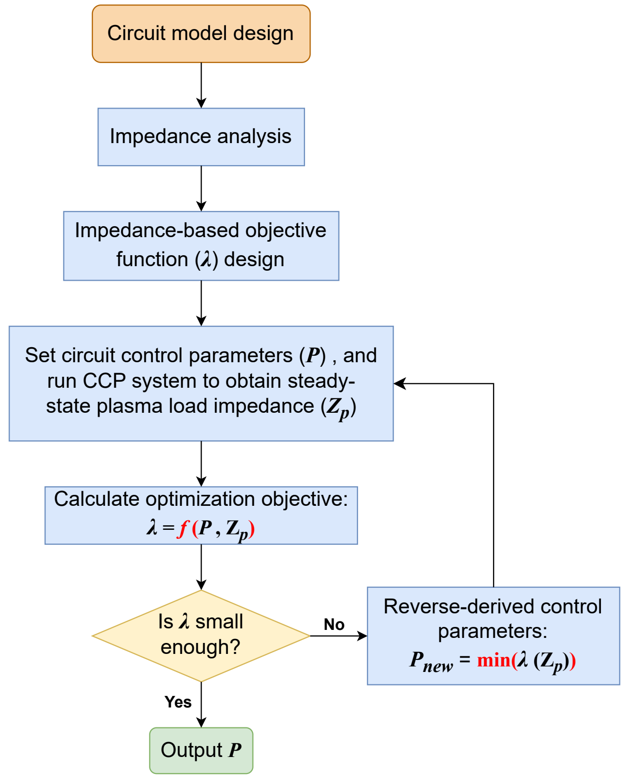

FIG. 1. The workflow for optimizing control parameters. P: The control parameter set. Z_p: The steady-state impedance of the plasma load. λ: The optimization objective. $min()$: The reverse reasoning algorithm to identify control parameters minimizing λ.

the total power loss in the circuit, with its value depending on the specific circuit configuration. (iii) A capacitively coupled plasma load, characterized by current I_p, voltage drop U_p, and complex impedance Z_p. To capture the dynamic changes during each RF cycle and highlight the details of the optimization process, we use a one-dimensional implicit PIC/MCC simulation[28–32] to model the plasma load. The simulation assumes pure argon as the working gas, with a gas temperature of 300 K and a pressure of p_{gas}. The electrode area is A_p, and the electrode spacing is D_p. The spatial and time step sizes are set to 3.125×10^{-4} m and 1.0×10^{-10} s, respectively. To accelerate steady-state convergence, the initial electron density between the plates is set to 1×10^{15} m^{-3}.

It is worth noting that the plasma model focuses on low-pressure conditions (below 10 Pa). Numerous studies have demonstrated that, under these conditions, direct ground-state ionization is the dominant process, while metastable particles have negligible impact on ionization in the plasma bulk[33–35]. To enhance computational efficiency, we exclude metastable particles from our simulation, which is consistent with prior studies[36,37]. The MCC model incorporates various collision processes, including electron elastic scattering, excitation, ionization, as well as ion elastic scattering and charge exchange. Given that the total ionization degree is less than 0.01%, we assume that neutral particles remain stationary and

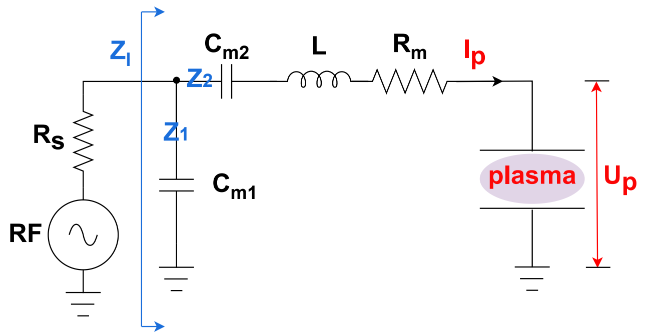

FIG. 2. The simulated network: plasma coupled with its external circuit. Z_l: Total load impedance. Z_1: Impedance of the C_{m1} branch. Z_2: Impedance of the C_{m2} branch. R_p and C_p: Equivalent resistance and capacitance of the plasma.

are uniformly distributed throughout the system. The simulation considers electron ionization and excitation collisions with Ar atoms, as well as elastic collisions of electrons and Ar^+ ions with Ar atoms. These collisions are modeled using random numbers and collision cross-sections. The electron and ion collision models are based on the work of Yamabe et al.[38] and Phelps et al.[39]. The interaction cross-sections are taken from the LXCat Phelps database[40]. For implementation details, see the code repository[41].

The plasma is self-consistently coupled to the external circuit through an iterative solution of Kirchhoff's law for the network shown in Fig. 2, alongside the PIC/MCC plasma simulation, while keeping the external circuit components unchanged. This modeling approach has been thoroughly validated in our previous studies[23,26,42–44]. As this paper focuses on the matching method, and as our optimization approach, which we will discuss later, is independent of specific modeling details, the external circuit coupling process and plasma model implementation are not discussed in depth here.

Step 2: Impedance analysis.

To achieve optimal impedance matching for the circuit shown in Fig. 2, we now perform an impedance analysis. First, the impedance of the power source is:

$$Z_s = R_s. \tag{1}$$

The total load impedance of the circuit can be expressed as:

$$Z_l = \frac{Z_1 Z_2}{Z_1 + Z_2}, \tag{2}$$

where:

$$Z_1 = Z_{C_{m1}} = \frac{1}{j\omega C_{m1}}, \tag{3}$$

$$\begin{aligned} Z_2 &= Z_{C_{m2}} + Z_L + Z_{R_m} + Z_p \\ &= \frac{1}{j\omega C_{m2}} + j\omega L + R_m + Z_p, \end{aligned} \tag{4}$$

j is the imaginary unit. $\omega = 2\pi f_s$, where f_s is the driving frequency. Z_p is the complex impedance of the plasma load, calculated from:

$$\begin{aligned} Z_p &= \frac{U_p}{I_p} e^{j\varphi} \\ &= \frac{U_p}{I_p}(\cos\varphi + j\sin\varphi), \end{aligned} \tag{5}$$

where U_p represents the amplitude of the voltage waveform across the plasma load, I_p represents the amplitude of the current waveform passing through it, and φ is the phase shift between the voltage and current waveforms. The corresponding amplitude and phase difference can be directly calculated from the original signal using the Hilbert transform[45,46].

The optimal impedance matching condition is:

$$Z_s = Z_l. \tag{6}$$

According to Eqs. (2) to (5), Z_l is a complex number and can be expressed as:

$$Z_l = R_l + jX_l, \tag{7}$$

where R_l and X_l are the real and imaginary parts, respectively. Similarly, Z_s is also a complex number but consists only of a real part, R_s. Therefore, the matching condition can be interpreted as the vector alignment between $(R_s, 0)$ and (R_l, X_l), leading to the following condition:

$$\vec{Z}_s(R_s, 0) = \vec{Z}_l(R_l, X_l). \tag{8}$$

Step 3: Impedance-based objective function design.

Based on the matching conditions specified in Eqs. (6) and (8), we introduce the following four optimization objectives. The first three focus on impedance matching, while the fourth aims to maximize the voltage drop across the plasma load. A summary of their key characteristics is provided in Table I.

- 1. Magnitude of the reflection coefficient, $|\Gamma|$.

  The reflection coefficient, denoted as Γ, is a complex-valued parameter that quantifies impedance mismatch in various systems, such as RF plasma system, antenna design, and transmission line theory[47–49]. However, directly using complex number as optimization objective can be cumbersome. Therefore, we typically use its magnitude as the optimization target instead, which is:

$$|\Gamma| = \left| \frac{Z_l - Z_s}{Z_l + Z_s} \right|, \tag{9}$$

  where Z_l represents the total load impedance of the system, and Z_s denotes the output impedance of the power source. The value of $|\Gamma|$ ranges from 0 to 1, with $|\Gamma| = 0$ indicating perfect power coupling (no reflection), and $|\Gamma| = 1$ indicating total reflection (no power coupling).

- 2. Modified impedance similarity, D'_{cs}.

TABLE I. Comparison of different optimization objectives for impedance matching.

Optimization Objectives	Description	Advantages	Disadvantages
$\|\Gamma\|$	The modulus of the reflection coefficient.	Standard industry metric for measuring impedance mismatch.	Only considers modulus, not phase.
D'_{cs}	Similarity between source impedance and total load impedance.	Considers both modulus and phase.	More complex calculation and difficult to differentiate.
D_e	Euclidean distance between source impedance vector and total load impedance vector.	Computationally convenient and geometrically intuitive.	Just the straight-line distance between two vectors, providing limited depiction of matching performance.
K	Amplification factor of power supply voltage.	Directly indicates the voltage drop across the plasma load; simple and direct measurement.	Highly complex derivation and computation; voltage alone does not fully characterize plasma.

D_{cs} is a parameter introduced in our previous work[26] to provide a more comprehensive assessment of matching effectiveness compared to $|\Gamma|$, considering both the magnitude and phase matching. To facilitate comparison with the changing trend of $|\Gamma|$, we modify the original calculation to:

$$\begin{aligned} D'_{cs} &= 1 - D_{cs} \\ &= 1 - \frac{\vec{Z}_l \cdot \vec{Z}_s}{||\vec{Z}_l|| * ||\vec{Z}_s||} * \frac{\min(||\vec{Z}_l||, ||\vec{Z}_s||)}{\max(||\vec{Z}_l||, ||\vec{Z}_s||)} \ . \end{aligned} \tag{10}$$

The value of D'_{cs} also ranges from 0 to 1. It is easy to prove that, in cases of perfect matching and total reflection, D'_{cs} aligns with $|\Gamma|$. In less-than-ideal matching scenarios, D'_{cs} provides a more precise assessment[26]. However, it is worth noting that the use of min() and max() functions in its definition makes it unsuitable for optimization algorithms that require differentiation.

- 3. Euclidean distance, D_e.

  The Euclidean distance, a fundamental concept in mathematics and applied sciences, quantifies the straight-line distance between two points in Euclidean space. For two points $\mathbf{p} = (p_1, \ldots, p_n)$ and $\mathbf{q} = (q_1, \ldots, q_n)$ in an n-dimensional Euclidean space, the distance is given by:

$$\begin{aligned} d(\mathbf{p}, \mathbf{q}) &= ||\vec{p} - \vec{q}|| \\ &= \sqrt{\sum_{i=1}^{n} (p_i - q_i)^2} \ . \end{aligned} \tag{11}$$

  For the two impedance matching vectors, Eq. (11) becomes:

$$\begin{aligned} D_e &= d(\mathbf{Z_l}, \mathbf{Z_s}) \\ &= ||\vec{Z}_l - \vec{Z}_s|| \\ &= \sqrt{(R_l - R_s)^2 + (X_l - 0)^2} \ . \end{aligned} \tag{12}$$

  From this definition, it is clear that D_e represents only the straight-line distance between two impedance vectors. When there is a mismatch, it may result from differences in magnitude, phase, or both. This easily leads to a situation where the same D_e value corresponds to different matching performances. Nonetheless, in a perfect match, the value of D_e approaches zero, consistent with $|\Gamma|$ and D'_{cs}. And compared to the previous two optimization objectives, this metric has the notable advantage of a straightforward geometric interpretation, making it easier to compute and understand. Furthermore, by framing impedance matching as the minimization of the distance between vectors $\vec{Z}_l$ and $\vec{Z}_s$, any distance metric - such as the Manhattan or Chebyshev distance[50] - can be used as an optimization objective.

- 4. Amplification factor of source voltage, K.

  For the circuit shown in Fig. 2, the voltage drop across the plasma load can be represented in terms of its impedance as:

$$\begin{aligned} U_p &= I_p * Z_p \\ &= (I_s - I_{C_{m1}}) * Z_p \\ &= (\frac{U_s}{Z_s + Z_l} - \frac{U_s - I_s * Z_s}{Z_{C_{m1}}}) * Z_p \\ &= (\frac{U_s}{Z_s + Z_l} - \frac{U_s - \frac{U_s * Z_s}{Z_s + Z_l}}{Z_{C_{m1}}}) * Z_p \\ &= U_s * \frac{Z_{C_{m1}} - Z_l}{(Z_s + Z_l) * Z_{C_{m1}}} * Z_p \ , \end{aligned} \tag{13}$$

  where $Z_{C_{m1}}$, Z_l, Z_s, and Z_p are as defined in Eqs. (2) to (5). Then, we can establish the relationship between the amplitude of U_p and U_s as:

$$\begin{aligned} |U_p| &= |U_s| * |\frac{Z_{C_{m1}} - Z_l}{(Z_s + Z_l) * Z_{C_{m1}}} * Z_p| \\ &= |U_s| * K \ , \end{aligned} \tag{14}$$

  where K is defined as the circuit's amplification factor for the power supply voltage. For a fixed power source, maximizing K also maximizes U_p, indicating improved matching.

Step 4: Activation of the CCP system.
For the circuit depicted in Fig. 2, we set the discharge parameters, such as the source output power, to fixed values.

TABLE II. Comparison of different minimization algorithms and their strategies.

Algorithms	Key Characteristics	Optimization Strategy
Grid Search (GS)	Simple, systematic evaluation of all possible parameter combinations over a defined range.	Exhaustive search ensuring comprehensive exploration of the parameter space.
Differential Evolution (DE)[51]	Robust, population-based metaheuristic using differential mutation; self-adaptive nature.	Evolves the population by scaling differences between randomly selected candidates; balances exploration and exploitation dynamically.
Gradient-based Optimizer (GBO)[52]	Novel algorithm combining gradient-based techniques[53] with population-based search.	Gradient Search Rule (GSR) for enhanced exploration and accelerated convergence; Local Escaping Operator (LEO) to avoid local optima.
Improved Dung Beetle Optimization (IDBO)[54,55]	Enhanced version of DBO[56] inspired by dung beetle behaviors; incorporates multiple strategic improvements.	Integrates chaotic maps, opposition-based learning, adaptive step sizes, and stochastic differential variation to enhance diversity and convergence precision.

This ensures that the system's matching state is solely determined by the values of the IMN components, which are designated as the control parameters. Traditional optimization methods typically rely on experience to select appropriate initial values for these control parameters to achieve convergence. In contrast, our optimization approach is independent of initial conditions, allowing the initial control parameters P (including C_{m1}, C_{m2}, and L) to be set randomly. After configuring these parameters, the CCP system is activated. Once steady-state is reached, the plasma impedance Z_p can be determined.

It is worth noting that in addition to computational methods — such as those based on Eq. (5) using the Hilbert transform to derive Z_p from voltage and current waveforms — plasma impedance can also be measured experimentally using techniques like RF probes and vector network analyzers (VNAs). RF probes (e.g., Langmuir probes), inserted into the plasma chamber, capture local voltage and current signals, enabling Z_p to be calculated as the amplitude ratio with phase difference, analogous to Eq. (5). VNAs, by injecting a small-signal RF sweep and analyzing reflection and transmission coefficients, characterize the system's overall impedance. Z_p can then be extracted by accounting for the matching network and external circuitry, as described in Eqs. (2)-(4). Both methods are widely validated and complement our simulation-based approach.

Step 5: Calculation of the optimization objective.

After obtaining the steady-state impedance of the plasma load, select a performance metric from Step 3, such as one of those listed in Table I, to serve as the optimization objective λ. With the discharge parameters fixed, the optimization objective can be expressed as:

$$\lambda = f(P, Z_p), \tag{15}$$

where P represents the control parameters and Z_p denotes the corresponding plasma impedance.

Step 6: Result output or re-optimization.

If the current optimization objective λ meets the desired threshold, the optimization is considered complete, and P is output as the optimal control parameter set. Otherwise, the impedance term Z_p in Eq. (15) is fixed, and an optimization algorithm min() is applied to inversely compute the control parameters that minimize λ. The resulting set, P_{new}, is then fed back into the system for further optimization.

In this step, the original matching problem has been entirely transformed into an algorithmic optimization problem for Eq. (15). The inverse reasoning algorithm min() can be any suitable algorithm. For instance, we briefly introduce several in Table II, including the basic brute-force grid search, the classic differential evolution algorithm, gradient descent, and the recently proposed Improved Dung Beetle Optimization algorithm. Alternatively, you may also opt for any other algorithms you are familiar with, such as machine learning or particle swarm optimization. The key point is that the goal is to apply these min() algorithms to estimate the control parameters P that minimize the optimization objective λ, and any algorithm that effectively achieves this can be chosen. Furthermore, as we will demonstrate in Sec. III B, the optimization results are independent of the specific algorithm used. Therefore, we will not delve into the detailed implementation of each algorithm, but rather summarize their key characteristics to highlight differences in their optimization strategies.

Step 7: Iteration until λ convergence.

The iterative process continues until λ reaches an acceptable value.

III. RESULT

Following the optimization workflow outlined above, this section details its implementation and application. Sec. III A presents a comprehensive example of the implementation process. Sec. III B explores how key elements of the workflow impact the optimization results. Sec. III C demonstrates the workflow's application under various discharge conditions.

A. Optimization Example for $|\Gamma|$

We choose the reflection coefficient magnitude, $|\Gamma|$, as the objective to illustrate the optimization process. For the CCP system shown in Fig. 2, we set the discharge parameters to the values listed in Table III. With these parameters fixed, the system is determined solely by the IMN and the plasma state, allowing Eq. (9) to be expressed as:

$$|\Gamma| = f(P, Z_p). \tag{16}$$

TABLE III. Discharge parameters of the simulation.

Types	Parameters	Value
Power source	f_s (MHz)	13.56
	P_s (W)	20
	R_s (Ω)	50
IMN	C_{m1} (pF), C_{m2} (pF), L (μH)	Tunable
	R_m (Ω)	5
Plasma load	p_{gas} (mTorr)	100
	A_p (m^2)	$\pi \times 0.1^2$
	D_p (m)	0.03

Next, the control parameters - C_{m1}, C_{m2} and L - are randomly initialized for the IMN as P_0 in Table IV. With P determined, the distribution of $|\Gamma|$ in the plasma's complex impedance space can be established based on Eq. (16). To better visualize and analyze this distribution, we map the complex impedance Z_p to its equivalent resistance R_p and capacitance C_p as follows:

$$\begin{aligned} R_p &= Re(Z_p) \\ C_p &= -\frac{1}{2\pi f_s \cdot Im(Z_p)}, \end{aligned} \tag{17}$$

where f_s is the driving frequency, Re() and Im() represent the real and imaginary parts, respectively. After the mapping, the $|\Gamma|$ distribution within the region $\{C_p \in (0\text{ pF},\ 150\text{ pF})\} \cap \{R_p \in (0\ \Omega,\ 90\ \Omega)\}$ is shown in Fig. 3(a1). As seen, almost the entire region is dominated by high reflection (red area), where $|\Gamma|$ approaches 1. We then use P_0 to run the CCP system, and the resulting spatiotemporal evolution of plasma density is shown in Fig. 3(a2). The vertical axis represents the distance from the upper electrode, and the horizontal axis denotes the RF cycles. It can be seen that the plasma density is notably low, indicating a very poor matching. As detailed in Table IV, the reflection coefficient is 0.9999, meaning nearly all incident power is reflected, with an absorption efficiency of only 0.001%. This low absorption leads to a plasma electron density of just $0.0302 \times 10^{16}\ m^{-3}$. The steady-state impedance of the plasma load is $Z_{p0} = (69.477\,\text{pF}, 9.321\,\Omega)$. We mark this position with a black cross in the corresponding complex impedance space (Fig. 3(a1)). At this location, Eq. (16) simplifies to:

$$|\Gamma| = f(P). \tag{18}$$

Using the DE algorithm from Table II, a new control parameter set, P_1, is identified (see Table IV), which brings $|\Gamma|$ close to zero. This completes the first optimization round.

By substituting P_1 into Eq. (16), we obtain an updated $|\Gamma|$ distribution, as illustrated in Fig. 3(b1). The figure shows that the adjustment of the IMN parameters ($P_0 \to P_1$) creates an ideal matching window ($|\Gamma| \approx 0$) at the plasma's steady-state position from the prior iteration, specifically at $Z_{\text{p}0}$, marked by a black star. The spatiotemporal evolution of the plasma is illustrated in Fig. 3(b2), where the plasma density remains low. However, significant improvements are evident when compared to the detailed data in Table IV: The CCP's reflection coefficient drops from 0.9999 to 0.9803, power absorption efficiency rises sharply from 0.001% to 1.080%, and the electron density increases from $0.0302 \times 10^{16}\text{m}^{-3}$ to $0.0560 \times 10^{16}\text{m}^{-3}$. These results demonstrate the effectiveness of the optimization. Similarly, by fixing the plasma at $Z_{\text{p}1}$ and minimizing the reflection coefficient $|\Gamma|$, we obtain another set, P_2, and its matching performance (see Table IV). Compared to P_1, the reflection coefficient decreases significantly ($0.9803 \to 0.3960$), power absorption efficiency improves nearly 25-fold ($1.080\% \to 25.261\%$), and electron density increasing almost 20-fold ($0.0560 \times 10^{16}\text{m}^{-3} \to 1.0416 \times 10^{16}\text{m}^{-3}$). From Fig. 3(c2), it is further evident that the plasma shows great improvements in energy coupling, stability, and uniformity. Importantly, Fig. 3(c1) shows that the plasma is now located at the edge of the ideal matching window, suggesting that the transition from the mismatched to the well-matched region accounts for the substantial progress achieved in this optimization step.

The iterative process continues until $|\Gamma|$ falls below an acceptable threshold. As shown in Table IV, by the P_8 iteration, the reflection coefficient magnitude of the CCP is quite small, reaching 0.0038, and the plasma demonstrates sufficient density and stability (see Fig. 3(d2)). Furthermore, as can be seen from Fig. 3(d1), the plasma is now almost entirely within the center of the ideal matching window, indicating that there is very limited space for further optimization. Therefore, the optimization is considered complete, and the IMN set, P_8, is identified as the optimal control parameter set.

Overall, the results in Fig. 3 clearly demonstrate the optimization process and direction of our method. By defining the impedance-based objective function in Eq. (16) and fixing the control parameter P, we made $|\Gamma|$ a function of Z_p, establishing the distribution of $|\Gamma|$ in the plasma load's complex impedance space (left column of Fig. 3). Meanwhile, the determination of P allows the plasma load to operate and reach a steady-state impedance position (Z_p) in this space. Once this position is identified, an algorithm back-calculates the control parameters to transform it into an optimal matching region. As a result, at each new optimization iteration, the ideal matching window always appears at the steady-state impedance position of the plasma determined in the previous iteration. While changes in control parameters alter the plasma state and subsequently shift its position in impedance space, our approach continuously tracks the plasma's updated position and adjusts the matching window accordingly. Once the window fully aligns with the plasma (like Fig. 3(d1)), optimal matching is achieved. Compared to traditional methods that adjust control parameters to bring the plasma load into the matching window, our method is like tying a wire to the plasma load,

TABLE IV. IMN parameters at different optimization iterations, and the corresponding steady-state matching performance. $|\Gamma|$: Magnitude of the reflection coefficient. η: Power absorption efficiency of the plasma. n_e: Electron density. Z_p: Steady-state impedance of the plasma load, where C_p is the corresponding equivalent capacitance and R_p is the corresponding equivalent resistance.

name	$C_{m1}(pF)$	$C_{m2}(pF)$	$L(\mu H)$	$\vert\Gamma\vert$[a]	η	$n_e(10^{16}\mathrm{m}^{-3})$	$Z_p(C_p(pF),R_p(\Omega))$
P_0	1591.90	9299.00	12.700	0.9999	0.001%	0.0302	(69.477, 9.321)
P_1	370.50	4415.39	2.279	0.9803	1.080%	0.0560	(30.541, 28.014)
P_2	168.37	7514.88	4.807	0.3960	25.261%	1.0416	(30.788, 9.438)
P_3	368.40	4560.07	4.771	0.0403	27.783%	1.1189	(30.684, 9.433)
P_4	368.49	5436.58	4.781	0.0159	28.374%	1.1306	(30.646, 9.439)
P_5	368.37	6824.17	4.781	0.0158	28.318%	1.1267	(30.611, 9.433)
P_6	368.48	8218.05	4.783	0.0046	28.884%	1.1512	(30.621, 9.438)
P_7	368.39	4468.67	4.796	0.0039	28.929%	1.1524	(30.627, 9.439)
P_8	368.38	9167.64	4.779	0.0038	28.907%	1.1522	(30.648, 9.439)

[a] The steady-state values of $|\Gamma|$, η, n_e, C_p and R_p are all obtained by taking the average over the last 2000 RF cycles.

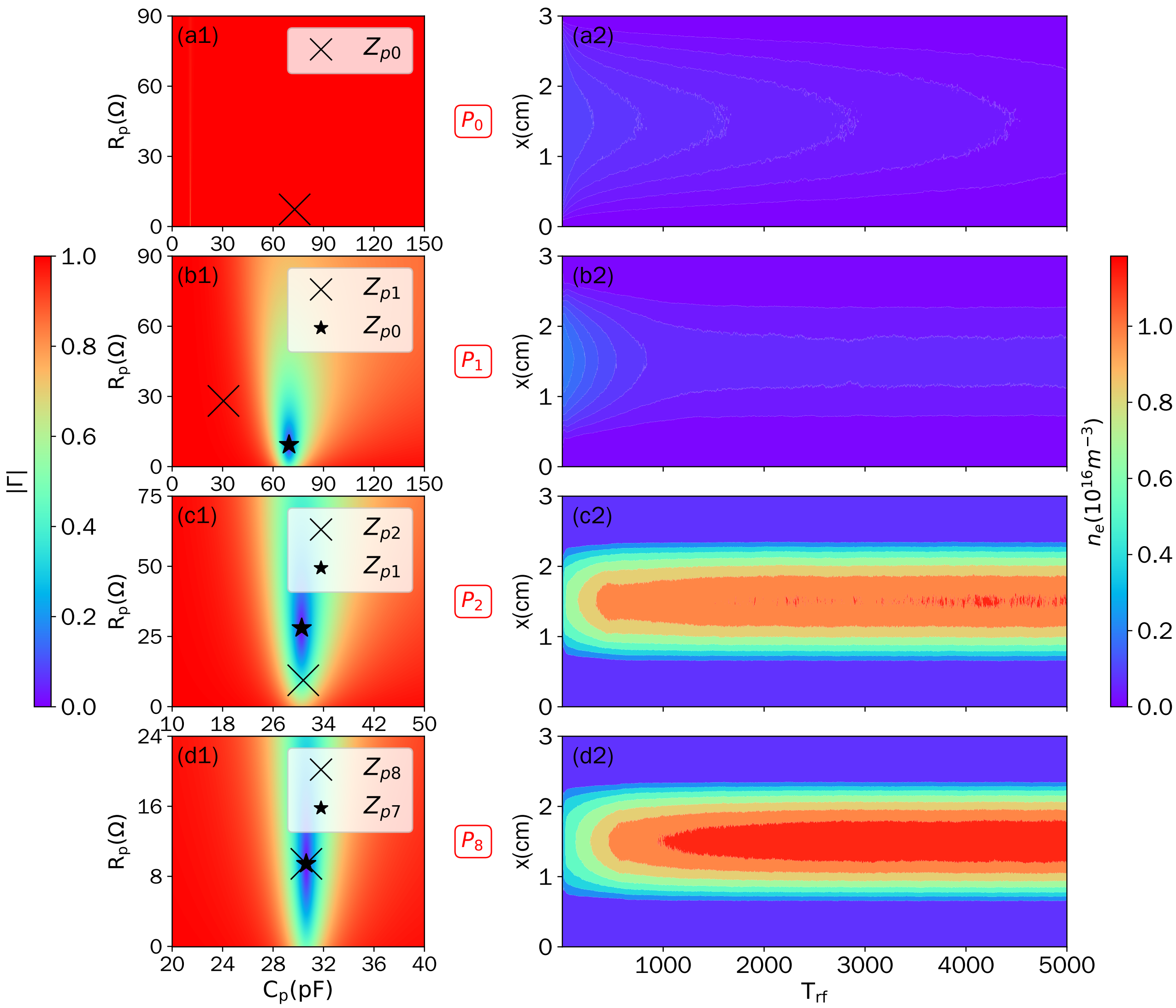

FIG. 3. Evolution of plasma for different control parameters from Table IV. Each row (a, b, c, d) corresponds to one set: P_0, P_1, P_2, and P_8, respectively. Left column (a1, b1, c1, d1): Reflection coefficient $|\Gamma|$ as a function of the plasma's equivalent capacitance C_p and resistance R_p. The black cross marks the steady-state impedance for the current control parameters; the black star, for the previous set. Right column (a2, b2, c2, d2): Spatiotemporal evolution of the plasma electron density. The vertical axis represents the distance from the upper electrode, and the horizontal axis denotes the RF cycles.

constantly pulling the matching window to its location. For a CCP system with a fixed power source, the plasma density it can sustain has an upper limit. As the matching condition improves, the plasma density approaches this limit, and its impedance converges to a specific value. Therefore, in the impedance space, our method ensures that the matching window can always be shifted to align with the plasma's convergent position, achieving optimal matching.

Additionally, another noteworthy phenomenon is observed: as shown in Table IV, the CCP matching performances converge after the sixth optimization round. However, the corresponding IMN component values do not converge. This indicates that the parameter sets P_6, P_7, and P_8 correspond to saddle points in the optimization landscape — points where the objective function $|\Gamma|$ achieves similar near-optimal values for different control parameter configurations due to the nonlinear relationship between the IMN parameters and the plasma impedance Z_p. In this context, saddle points allow multiple IMN configurations to align the total load impedance Z_l with the source impedance Z_s, yielding comparable matching performance. These saddle points will be discussed in detail in the following section.

B. Analysis of Key Optimization Elements

As illustrated in Fig. 1, our optimization method involves four key elements: the control parameter P, the steady-state impedance of the plasma load Z_p, the optimization objective λ, and the reverse reasoning algorithm $min()$, all of which are decisive in determining the optimization outcomes.

We first examine how varying initial control parameters and optimization objectives affect the results. As shown in Fig. 4(a), 10 sets of initial IMN values are randomly generated in the parameter space $\{C_{m1} \in (0\text{ pF},\ 10000\text{ pF})\} \cap \{C_{m2} \in (0\text{ pF},\ 10000\text{ pF})\} \cap \{L \in (0\ \mu\text{H},\ 100\ \mu\text{H})\}$, and each set of parameters will be optimized under different optimization objectives. Fig. 5 shows the entire optimization process, where subfigures (a)-(c) depict the changes in IMN control parameters during each iteration, and subfigures (d)-(i) illustrate the changes in the CCP system's matching performance, including the electron density at the center of the electrodes (n_e), voltage drop across the plasma load (U_p), amplification factor of power supply voltage (K), power absorption efficiency of the plasma load (η), magnitude of the reflection coefficient ($|\Gamma|$), and the average electron temperature between electrode plates (T_e). Finally, the distribution of the best-matching parameters obtained is presented in Fig. 4(b).

As shown in Fig. 5(a)-(c), starting from the 10 initial sets (iteration 0), the values of C_{m1} and L quickly converge to nearly identical levels after just two iterations, regardless of the optimization objectives. In contrast, C_{m2} exhibits a markedly different behavior, with no clear convergence trend observed. By the end of the optimization process, C_{m2} values remain highly variable, depending on the initial conditions and objectives. This disparity is further illustrated in Fig. 4(b), where C_{m1} is concentrated around 368.4 pF, L around 4.82 μH, and C_{m2} is widely distributed within the initial range of

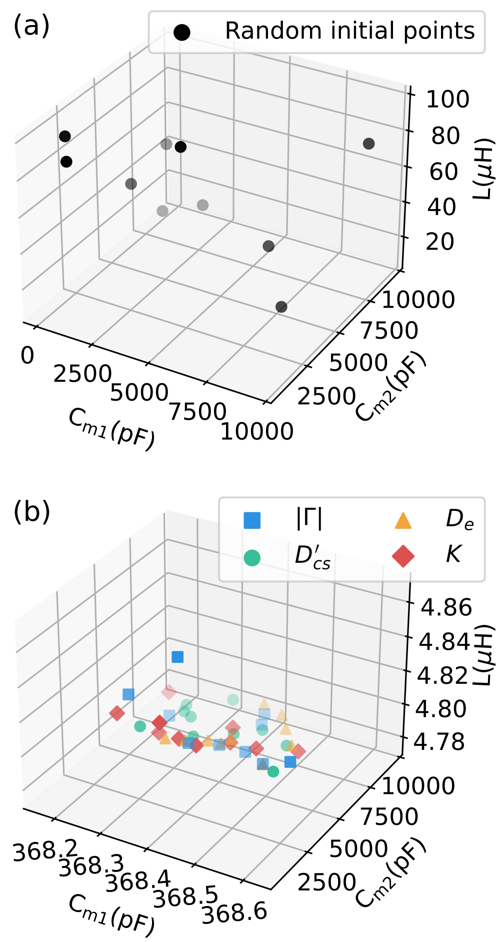

FIG. 4. IMN control parameter variations before and after optimization: (a) Ten randomly generated initial control parameter sets. (b) Optimal control parameters identified under different optimization objectives.

0 to 10,000 pF. Despite the lack of convergence for C_{m2}, the overall matching performance of the CCP system improves progressively with each iteration, stabilizing after six rounds, as shown in Fig. 5(d)-(i). This suggests that, even with scattered distribution, all the points shown in Fig. 4(b) represent saddle points that provide similarly optimal matching performance. This observation aligns with the results presented in Table IV.

From the optimization processes in Sec. III A, it can be observed that the new IMN parameters are reverse-derived from Eq. (16) via an algorithm after fixing the plasma's position in (C_p, R_p) space. Consequently, any slight variations in the equation, such as changes in plasma impedance or adjustments in the optimization algorithm, can result in different control parameters. Given that it is nearly impossible to find two completely identical plasma states in a CCP system, even with identical control parameters, subtle variations in plasma behavior may occur due to environmental noise and random factors. Thus, even within the center of the ideal matching window, the plasma's steady-state position will still

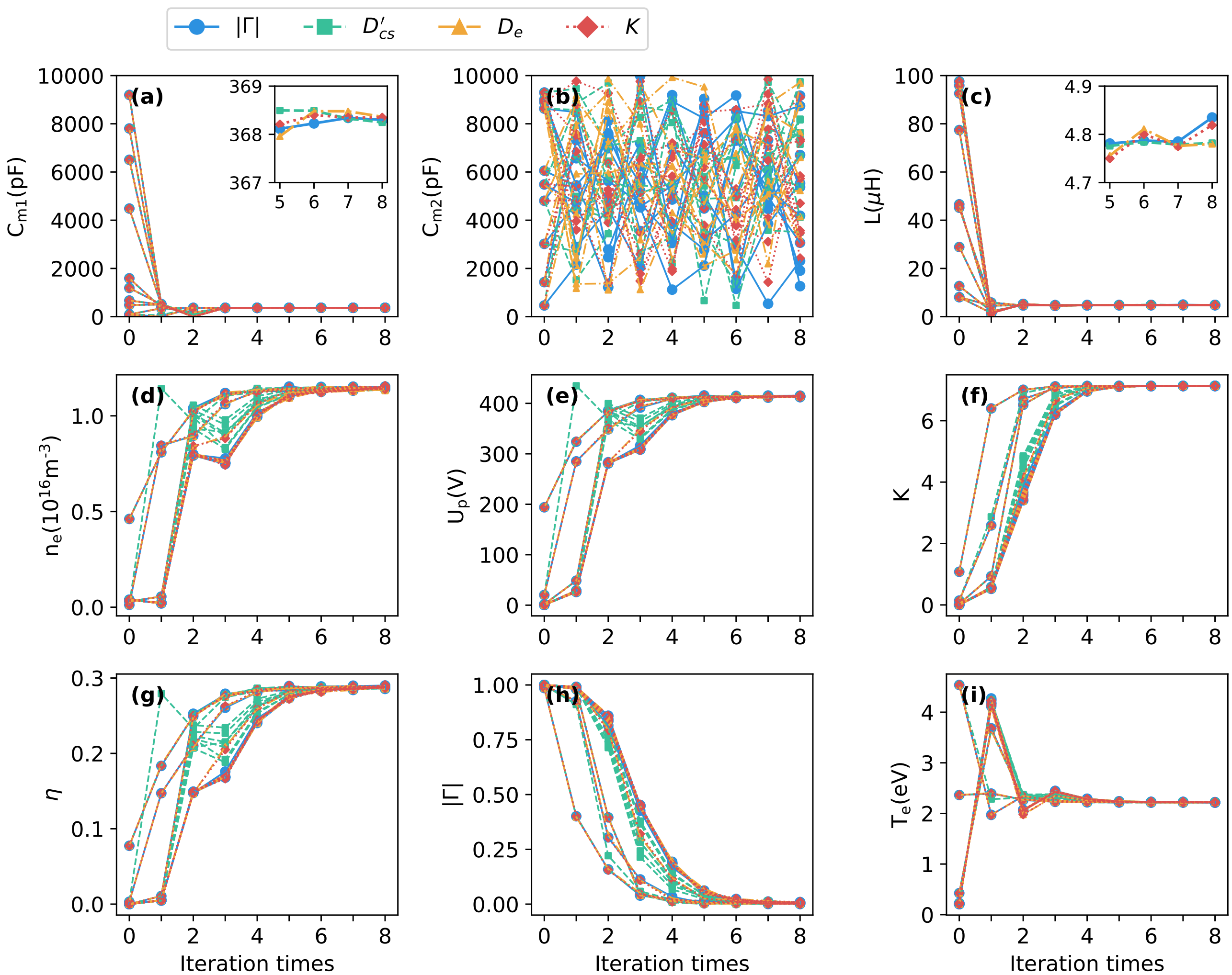

FIG. 5. Changes in IMN components and plasma performances at each optimization iteration for different optimization objectives. (a), (b), (c): Values of three IMN components: C_{m1}, C_{m2}, and L. (d) Electron density at the center of the electrode plates. (e) Voltage drop across plasma load. (f) Amplification factor of power supply voltage, defined by Eq. 14. (g) Power absorption efficiency of plasma load, defined as $\eta = P_p/P_s$. (h) Magnitude of reflection coefficient. (i) Average electron temperature between electrode plates.

exhibit slight deviations, which naturally leads to the possibility of finding different IMN parameters. This explains why, starting with 10 distinct initial control parameters and 4 optimization objectives, the saddle points shown in Fig. 5(a)-(c) evolve along unique trajectories, ultimately producing 40 saddle points, as illustrated in Fig. 4(b).

Therefore, it is clear that the emergence of saddle points is closely linked to the small perturbations in the variables of Eq. (16). To further explore this phenomenon, here we perform a sensitivity analysis of the equation to explain why the distribution of saddle points differs among the control components, i.e., concentrated on C_{m1} and L, but divergent on C_{m2}. As shown in Table IV and Fig. 3, as the plasma matching performance converges, the plasma position within the (C_p, R_p) space stabilizes. We designate the averaged coordinates of P6, P7, and P8, located at (30.632 pF, 9.439 Ω), as the convergence point. To examine the potential plasma convergence locations, we define a region around this point with a $\pm 5\%$ interval for each coordinate. To simulate small deviations at each convergence location, Gaussian noise with a mean of 0 and a standard deviation of 0.001 is applied to points within this region. The parameter space of IMN remains consistent with Fig. 4(a), i.e., $\{C_{m1} \in (0\text{ pF},\ 10000\text{ pF})\} \cap \{C_{m2} \in (0\text{ pF},\ 10000\text{ pF})\} \cap \{L \in (0\ \mu\text{H},\ 100\ \mu\text{H})\}$. Fig. 6 displays the results: The first row shows the expected values of the optimal IMN components across different steady-state positions, highlighting the effect of plasma convergence position on the optimal control parameters. The second row depicts the corresponding standard deviations, emphasizing the impact of noise. Subplots (a1) and (c1) reveal that for components C_{m1} and L, plasma impedance variation does not affect their convergence; their values stabilize at approximately 368 pF and 4.8 μH, respectively. The small standard deviations further indicate a narrow distribution around the mean, reflecting

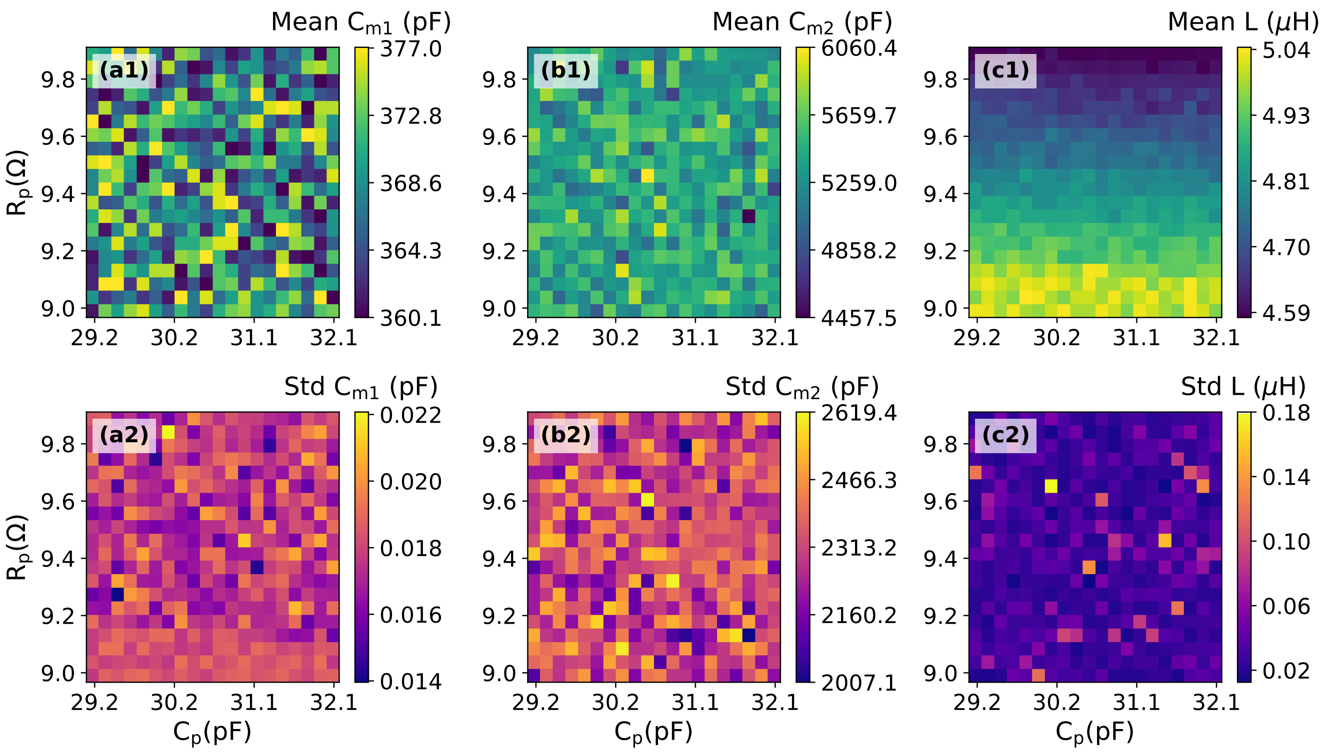

FIG. 6. Sensitivity analysis of IMN parameters on plasma convergence position and noise in (C_p, R_p) space. (a1), (b1), (c1): Expected values of the optimal matching components C_{m1}, C_{m2}, and L, respectively, under varying C_p and R_p conditions. (a2), (b2), (c2): Corresponding standard deviations for C_{m1}, C_{m2}, and L, respectively.

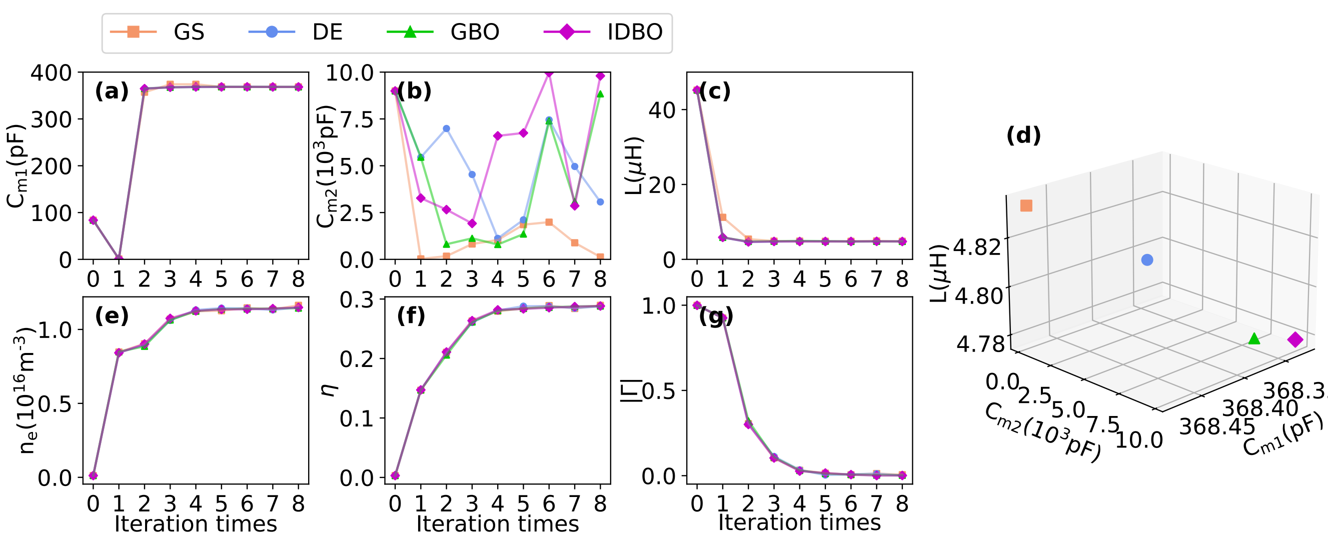

FIG. 7. Optimization processes corresponding to different algorithms for the same set of initial IMN parameters. (a), (b), (c): Changes in IMN parameters. (d): Distribution of the IMN parameters corresponding to the 8th iteration. (e), (f), (g): Changes in electron density, power absorption efficiency of CCP, and magnitude of reflection coefficient.

minimal sensitivity to noise. This insensitivity to the plasma impedance deviations explains the convergence behavior of C_{m1} and L observed in Fig. 5. Conversely, C_{m2} in Fig. 6(b1) and (b2) exhibits significant fluctuations in both mean and standard deviation across positions, demonstrating high sensitivity to plasma impedance and noise, which leads to its divergence in Fig. 5. In other words, the plasma's impedance offset within the matching window causes the emergence of saddle points, while the varying sensitivity of different components to this offset results in diverse saddle point distributions.

Next, we analyze how reverse reasoning algorithms impact the results. Fig. 7 shows the optimization results obtained by various algorithms listed in Table II for the same optimization objective $|\Gamma|$, and the same initial control parameter set: $(C_{m1},\ C_{m2},\ L) = (83.73\ \text{pF},\ 8994.40\ \text{pF},\ 45.20\ \mu\text{H})$. From subplots (a)-(c), it is evident that the evolution trajectories of the IMN control parameters differ across algorithms due to variations in optimization strategies. As a result, in subplot (d), the four algorithms each yield a distinct optimal matching parameter set, with their values aligning with the range shown in Fig. 4(b). Interestingly, despite differences in the iterative adjustments of control parameters, the matching performance trajectories shown in subplots (e)-(g) exhibit remarkable consistency, with nearly overlapping curves. This suggests that the effectiveness of our matching method is largely unaffected by the choice of optimization algorithm, provided the algorithm reliably minimizes the objective. This is straightforward: While different algorithms employ distinct optimization strategies, they share the same optimization goal. These algorithms are simply tools for finding control parameters that minimize the objective, and as long as the minimization level is consistent, the matching results will align. In other words, inconsistencies in matching results across steps in Fig. 7 would arise only if the objective minimization levels differ, for instance, one algorithm reaching a 10^{-2} level and another a 10^{-4} level.

Overall, for the four elements discussed in Fig. 1, the definition of the optimization objective λ establishes the functional relationship between the optimal matching window and circuit parameters, then the choice of control parameters P directly determines the steady-state position of the plasma in Z_p space. Since our strategy is using an inference algorithm $min()$ to adjust the control parameters, aiming to convert this position into a matching window, any change in these four elements can lead to different control parameters, which explains the emergence of saddle points. Additionally, since IMN components vary in sensitivity to the plasma impedance shifts - some highly responsive, others less so - saddle point distributions differ accordingly. Sensitive components show divergent distributions, while less sensitive ones converge. This variation offers key insights for designing more efficient, component-specific matching strategies. Specifically, for components with clustered saddle points, precise fine-tuning is critical, while for components with broader distributions, coarse adjustments are sufficient, as there is always an opportunity to encounter the next saddle point.

C. Performance Across Different Discharge Conditions

The results above present the optimization outcomes under the fixed discharge conditions listed in Table III. Using these values as a baseline, we extended the optimization approach to various discharge conditions and analyzed the corresponding optimal matching states. In Fig. 8, we illustrate the different optimal matching states identified by our method for three discharge parameters: power supply output (P_s), driving frequency (f_s) and plasma load electrode area (A_p). The parameter adjustment is implemented using a scaling factor. For example, with a baseline P_s of 20 W from Table III, a scaling factor of 1 corresponds to 20 W, while 0.95 corresponds to $0.95 \times 20 = 19$ W. When one parameter is adjusted, the others remain fixed. Subfigure (a) illustrates the changes in plasma steady-state capacitance and resistance under optimal matching conditions, with arrows indicating the trend as the scaling factor increases from 0.8 to 1.2. Subfigures (b)-(d) show the optimal IMN control parameters for different scaling factors. Subfigures (e)-(h) present the variations in power transmission-related parameters, including the power supplied by the source (P_s), the voltage drop across the plasma load (U_p), the current through the plasma load (I_p), and the power absorbed by the plasma load (P_p). Subfigures (i)-(l) display the variations in key plasma matching parameters, including the source voltage amplification factor (K), plasma power absorption efficiency (η), electron density at the center of the electrodes (n_e), and the average electron temperature between the electrodes (T_e).

We begin by analyzing how optimal matching states vary with different power supply outputs (P_s). As shown in Fig. 8(a), the plasma impedance under optimal matching conditions remains close to the baseline value across various scaling factors, indicating that changes in power output have minimal impact on the optimal matching state. This is further supported by the consistent IMN control parameters in subfigures (b) and (d). Additionally, the plasma's power transmission parameters - U_p, I_p, and P_p - exhibit a linear relationship with the source power (P_s), the voltage amplification factor in subfigure (i) and the power absorption efficiency in subfigure (j) remain nearly unchanged. These findings suggest that in a CCP system under optimal matching, the source power output minimally affects the energy coupling dynamics, allowing plasma-absorbed energy to scale directly with supplied energy. Furthermore, in subfigure (l), we observe that the average electron temperature between the electrodes decreases as the power increases. This trend is attributed to the rise in plasma density, which leads to more frequent electron-neutral collisions. These collisions distribute energy across a larger electron population, thereby reducing the average energy per electron[57,58].

Next, we investigate the influence of the driving frequency (f_s). As shown in Fig. 8(a), increasing f_s makes the plasma load less resistive and more capacitive. To maintain optimal matching, the IMN control parameters must adjust, as illustrated in subfigures (b)-(d). This adjustment reduces K (Fig. 8(i)) via Eq. (14). This adjustment reduces K (Fig. 8(i)) via Eq. (14). As K decreases, U_p also declines, and this drop surpasses the increase in I_p, resulting in a net decrease in P_p. Therefore, at optimal matching, higher driving frequencies result in lower plasma power absorption, as shown in Fig. 8(h). Interestingly, despite this lower absorbed power, subfigures (k) and (l) show an increase in steady-state electron density and temperature. This can be attributed to two factors: First, at higher driving frequencies, the rapid oscillations of the electric field enhance stochastic heating efficiency, allowing electrons to gain energy more effectively from the oscillating sheath boundaries. This process improves

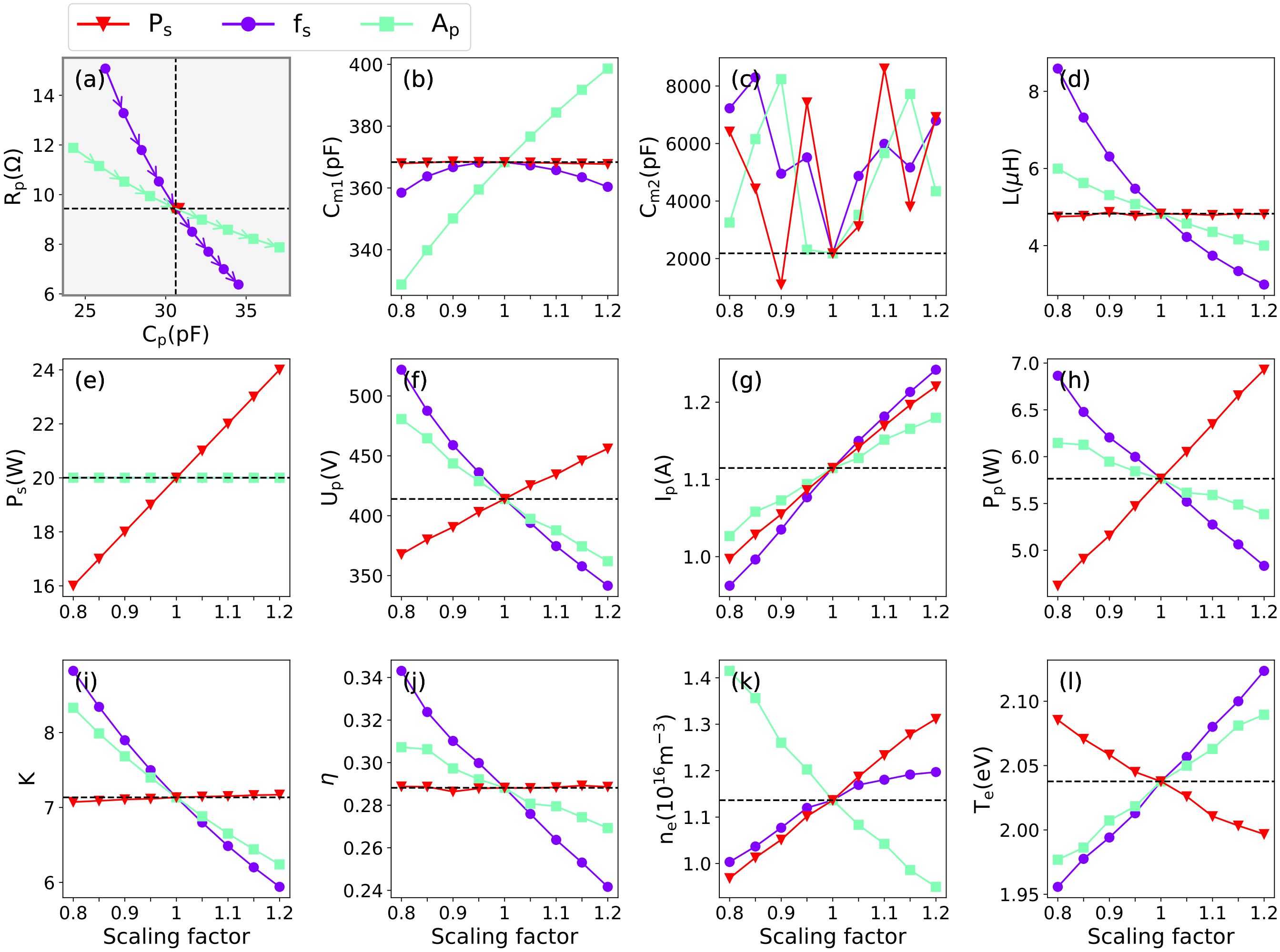

FIG. 8. Variation of optimal matching states across varying discharge parameters and scaling factors. Parameters studied include source power output (P_s), driving frequency (f_s), and plasma load electrode area (A_p), with scaling factors ranging from 0.8 to 1.2. In each subfigure, the dashed line represents the baseline value at a scaling factor of 1. (a): Steady-state position of the plasma in impedance space, with arrows indicating trends as the scaling factor increases. (b), (c), (d): Optimal IMN parameters versus scaling factor. (e), (f), (g), (h): Power output from the source, voltage drop across the plasma load, current through the plasma load, and power absorbed by the plasma. (i), (j), (k), (l): Circuit voltage amplification factor (see Table I), plasma power absorption efficiency ($\eta = P_p/P_s$), electron density at the plasma electrode center, and average electron temperature between the electrodes. Note: Subfigure (a) depicts the steady-state impedance variation, with horizontal and vertical axes representing plasma load equivalent capacitance and resistance, respectively. Unlike other subfigures showing a single variable's change, (a) involves two variables, hence its background is shaded in gray for distinction.

electron confinement and reduces ion losses to the electrodes, leading to higher electron density, particularly when the driving frequency is below the threshold frequency[59,60]. Second, at lower frequencies, energy dissipation mainly affects ions due to their higher mass and lower mobility. As the frequency increases, however, energy dissipation shifts to the lighter, more mobile electrons, equiring less energy and resulting in higher electron temperatures[61,62]. These results suggest that when operating under optimal matching conditions, higher frequencies improve CCP ionization efficiency, enabling higher electron density and temperature with lower power consumption[13,63,64].

Finally, we examine the influence of an internal plasma parameter, the electrode area of the plasma load (A_p). As shown in Fig. 8, increasing A_p has a similar effect to increasing f_s: both make the plasma load less resistive and more capacitive, and both decrease the optimally matched absorbed power. However, unlike f_s, a larger A_p decreases electron density while increasing electron temperature, as illustrated in Fig. 8(k) and Fig. 8(l). In contrast to higher driving frequencies, which boost ionization efficiency despite lower power, expanding the electrode area does not enhance ionization. Instead, it simply leads to lower electron density due to decreased power absorption. Yet, as reported by Gahan et al.[65], enlarging the electrode area also expands the sheath region, intensifying stochastic heating as electrons gain energy from oscillating electric fields within the sheath. This shift in power absorption from the plasma bulk to the sheath - where stochastic heating is more effective - raises overall electron energy. Consequently, a larger electrode area leads to lower electron density and higher average electron temperature.

In previous studies, the power absorption efficiency, η, has commonly been used as a metric to compare the performance of various matching conditions. However, as shown in Fig. 8(j), η varies with changes in discharge parameters such as the driving frequency, even when the system remains in the optimal matching state. Therefore, parameters like η are not suitable for evaluating the matching performance across systems with different discharge conditions. Moreover, although driving frequency tuning is a commonly used matching method, changes in frequency affect the plasma's energy utilization, resulting in different steady-state impedance values of the plasma load (see Fig. 8(a)). In other words, if the driving frequency continuously fluctuates, the convergence position of the plasma in the impedance space will shift accordingly. As discussed in Sec. III A, our method ensures convergence only when the plasma reaches a fixed impedance convergence point, allowing its position to be tracked. Therefore, the driving frequency, like other discharge parameters influencing the convergence impedance of the plasma load, cannot serve as an optimization parameter alongside the IMN control parameters. This distinction highlights the fundamental difference between frequency tuning and IMN tuning for achieving impedance matching.

IV. CONCLUSIONS

In this paper, we have presented a novel and robust method for optimizing the control parameters in CCP systems. Unlike traditional optimization methods that operate within the control parameter space, our approach transitions the optimization process to the plasma impedance space, where control parameters are inversely inferred. In this framework, the plasma's equivalent impedance not only serves as a bridge linking new and old control parameters, decoupling the control parameters from their historical paths, but also serves as a bridge linking the CCP system and the optimization algorithm, decoupling the latter from specific device configurations and ensuring consistency across 1D, 2D, and 3D simulations, as well as experimental setups.

This paper begins with a detailed description of the optimization workflow. Then using the optimization of the reflection coefficient modulus as an example to illustrate the implementation process, highlighting the natural emergence of saddle points and analyzing the guaranteed convergence of our method. Subsequently, we investigate four key factors in the optimization methods and reveal that the emergence of saddle points is due to plasma impedance's slight deviations within the ideal matching window. Furthermore, a sensitivity analysis of the optimization objective function explain the distribution of saddle points across different components: some components show a concentrated distribution of saddle points, while others exhibit a more dispersed distribution. Finally, by comparing optimization results under different discharge conditions, we reveal that parameters like plasma power absorption efficiency can vary even under optimal matching conditions. This indicates that such parameters are unsuitable for evaluating matching performances across different discharge conditions. We also clarify the key differences between the two common matching methods in the CCP system: driving frequency tuning and IMN components tuning.

In conclusion, despite the highly decoupled and straightforward optimization process, the proposed method demonstrates strong effectiveness, efficiency, and robustness across various scenarios, highlighting its potential as a valuable tool for optimizing CCP-based industrial processes. Future research will aim to extend this approach to more complex configurations, such as dual-frequency or multi-frequency CCP systems, and to explore its applicability in other plasma applications.

ACKNOWLEDGEMENT

This work was supported by the National Natural Science Foundation of China (12275095, 11975174 and 12011530142).

AUTHOR DECLARATIONS

Conflict of interest

The authors have no conflicts to disclose. Wei Jiang, Dehen Cao and Shimin Yu have issued a Patent, pending.

DATA AVAILABILITY STATEMENT

The data that support the findings of this study are available from the corresponding author upon reasonable request.

ORCIDS

Dehen Cao https://orcid.org/0009-0006-8038-9176
Shimin Yu https://orcid.org/0000-0002-3832-5252
Hongyu Wang https://orcid.org/0009-0007-8100-1409
Zhipeng Chen https://orcid.org/0000-0002-8330-0070
Wei Jiang https://orcid.org/0000-0002-9394-585X
Ya Zhang https://orcid.org/0000-0003-0473-467X

REFERENCES

[1]Z.-h. Bi, Y.-x. Liu, W. Jiang, X. Xu, and Y.-n. Wang, "A brief review of dual-frequency capacitively coupled discharges," Current Applied Physics **11**, S2–S8 (2011).
[2]Z. Gao, Z. Wu, S. Zhao, T. Zhang, and Q. Wang, "Enhanced capacitive property of hfn film electrode by plasma etching for supercapacitors," Materials Letters **235**, 148–152 (2019).

[3]H. J. Kim, J. S. Kim, and H. J. Lee, "Numerical analysis for optimization of the sidewall conditions in a capacitively coupled plasma deposition reactor," Journal of Applied Physics **126**, 173301 (2019).
[4]H. J. Kim, K. Lee, and H. Park, "Numerical optimization of dielectric properties to achieve process uniformity in capacitively coupled plasma reactors," Plasma Sources Science and Technology **33**, 015008 (2024).
[5]F. Beckfeld, M. Janssen, C. Neuroth, I. Korolov, and J. Schulze, "Fiber proes: Phase resolved optical emission spectroscopy via optical fibers for knowledge-based plasma process development and monitoring," Review of Scientific Instruments **96**, 033507 (2025).
[6]S.-Z. Li, H. Li, J. Zhang, S. Wang, Y.-X. Wang, and Z.-J. Jin, "Effect of transmission line on impedance matching of atmospheric-pressure radio-frequency capacitive microplasma discharge," IEEE Transactions on Plasma Science **42**, 1654–1660 (2014).
[7]W. Sun, X. Qin, S. Wang, and Y. Li, "General guided-wave impedance-matching networks with waveguide-metamaterial elements," Physical Review Applied **18**, 034070 (2022).
[8]G. Cheng, Z. Li, L. Luo, Z. Wang, X. He, and B. He, "A low power and high gain current-reused lna using cascaded l-type input matching network," Microelectronics Journal **75**, 15–26 (2018).
[9]G. Han, Y. Liu, Q. Li, Z. Xing, and Z. Zhang, "A 6.78-mhz distance-insensitive wireless power transfer system with a dual-coupled l-type matching network," Review of Scientific Instruments **92**, 054705 (2021).
[10]R. Sinha and A. De, "Theory on matching network in viewpoint of transmission phase shift," IEEE Transactions on Microwave Theory and Techniques **64**, 1704–1716 (2016).
[11]S. Yu, F. Cheng, C. Gu, C. Wang, and K. Huang, "Compact and efficient broadband rectifier using t-type matching network," IEEE Microwave and Wireless Components Letters **32**, 587–590 (2022).
[12]T. C. Beh, M. Kato, T. Imura, S. Oh, and Y. Hori, "Automated impedance matching system for robust wireless power transfer via magnetic resonance coupling," IEEE Transactions on Industrial Electronics **60**, 3689–3698 (2013).
[13]S. Sharma, N. Sirse, P. K. Kaw, M. M. Turner, and A. R. Ellingboe, "Effect of driving frequency on the electron energy distribution function and electron-sheath interaction in a low pressure capacitively coupled plasma," Physics of Plasmas **23**, 110701 (2016).
[14]K. Takahashi, Y. Nakano, and A. Ando, "Frequency-tuning radiofrequency plasma source operated in inductively-coupled mode under a low magnetic field," Journal of Physics D: Applied Physics **50**, 265201 (2017).
[15]B. Wang and Z. Cao, "A review of impedance matching techniques in power line communications," Electronics **8**, 1022 (2019).
[16]S. Sharma, N. Sirse, A. Kuley, A. Sen, and M. M. Turner, "Driving frequency effect on discharge parameters and higher harmonic generation in capacitive discharges at constant power densities," Journal of Physics D: Applied Physics **54**, 055205 (2020).
[17]V. C. Parro and F. M. Pait, "An automatic impedance matching system for a multi point power delivery continuous industrial microwave oven," in *Proceedings of the 2004 IEEE International Conference on Control Applications* (IEEE, Taipei, Taiwan, 2004) pp. 143–148.
[18]J. Franek, S. Brandt, B. Berger, M. Liese, M. Barthel, E. Schüngel, and J. Schulze, "Power supply and impedance matching to drive technological radio-frequency plasmas with customized voltage waveforms," Review of Scientific Instruments **86**, 053504 (2015).
[19]J. Wang, S. Dine, J.-P. Booth, and E. V. Johnson, "Experimental demonstration of multifrequency impedance matching for tailored voltage waveform plasmas," Journal of Vacuum Science & Technology A **37**, 021303 (2019).
[20]A. Khomenko and S. Macheret, "Capacitively coupled discharge as a tunable impedance element for rf systems," Journal of Applied Physics **128**, 173301 (2020).
[21]Z. V. Missen, S. Macheret, A. Semnani, and D. Peroulis, "Plasma switch-based technology for high-speed and high-power impedance tuning," in *2021 IEEE 21st Annual Wireless and Microwave Technology Conference (WAMICON)* (IEEE, Sand Key, FL, USA, 2021) pp. 1–4.
[22]F. Schmidt, T. Mussenbrock, and J. Trieschmann, "Consistent simulation of capacitive radio-frequency discharges and external matching networks," Plasma Sources Science and Technology **27**, 105017 (2018).
[23]S. Yu, Z. Chen, H. Wu, L. Guo, Z. Wang, W. Jiang, and Y. Zhang, "Best impedance matching seeking of single-frequency capacitively coupled plasmas by numerical simulations," Journal of Applied Physics **132**, 083302 (2022).
[24]S. Yu, Z. Chen, J. Xu, H. Wang, L. Wang, Z. Wang, W. Jiang, J. Schulze, and Y. Zhang, "Impedance matching design for capacitively coupled plasmas considering coaxial cables," Journal of Physics D: Applied Physics **57**, 475204 (2024).
[25]P. Tian, J. Kenney, S. Rauf, I. Korolov, and J. Schulze, "Uniformity of low-pressure capacitively coupled plasmas: Experiments and two-dimensional particle-in-cell simulations," Physics of Plasmas **31**, 043507 (2024).
[26]D. Cao, S. Yu, Z. Chen, Y. Wang, H. Wang, Z. Chen, W. Jiang, and Y. Zhang, "Optimizing impedance matching parameters for single-frequency capacitively coupled plasma via machine learning," Journal of Vacuum Science & Technology A **42**, 013001 (2024).
[27]Q. Yuan, Z. Liu, G. Yin, and J. Ren, "Higher order harmonics are suppressed in rf capacitively coupled ar plasmas using an external impedance circuit," IEEE Transactions on Plasma Science **52**, 2826–2836 (2024).
[28]J. U. Brackbill and D. W. Forslund, "An implicit method for electromagnetic plasma simulation in two dimensions," Journal of Computational Physics **46**, 271–308 (1982).
[29]B. I. Cohen, A. B. Langdon, and A. Friedman, "Implicit time integration for plasma simulation," Journal of Computational Physics **46**, 15–38 (1982).
[30]H.-y. Wang, W. Jiang, and Y.-n. Wang, "Implicit and electrostatic particle-in-cell/monte carlo model in two-dimensional and axisymmetric geometry: I. analysis of numerical techniques," Plasma Sources Science and Technology **19**, 045023 (2010).
[31]H. Wu, Y. Zhou, J. Gao, Y. Peng, Z. Wang, and W. Jiang, "Electrical breakdown in dual-frequency capacitively coupled plasma: A collective simulation," Plasma Sources Science and Technology **30**, 065029 (2021).
[32]M. M. Turner, A. Derzsi, Z. Donkó, D. Eremin, S. J. Kelly, T. Lafleur, and T. Mussenbrock, "Simulation benchmarks for low-pressure plasmas: Capacitive discharges," Physics of Plasmas **20**, 013507 (2013).
[33]D.-Q. Wen, J. Krek, J. T. Gudmundsson, E. Kawamura, M. A. Lieberman, P. Zhang, and J. P. Verboncoeur, "On the importance of excited state species in low pressure capacitively coupled plasma argon discharges," Plasma Sources Science and Technology **32**, 064001 (2023).
[34]M. Roberto, H. B. Smith, and J. P. Verboncoeur, "Influence of metastable atoms in radio-frequency argon discharges," IEEE Transactions on Plasma Science **31**, 1292–1298 (2003).
[35]L. Lauro-Taroni, M. M. Turner, and N. S. Braithwaite, "Analysis of the excited argon atoms in the gec rf reference cell by means of one-dimensional pic simulations," Journal of Physics D: Applied Physics **37**, 2216 (2004).
[36]L. Wang, P. Hartmann, Z. Donkó, Y.-H. Song, and J. Schulze, "Effects of structured electrodes on electron power absorption and plasma uniformity in capacitive rf discharges," Journal of Vacuum Science & Technology A **39**, 063004 (2021).
[37]B. Zheng, Y. Fu, D.-q. Wen, K. Wang, T. Schuelke, and Q. H. Fan, "Influence of metastable atoms in low pressure magnetized radio-frequency argon discharges," Journal of Physics D: Applied Physics **53**, 435201 (2020).
[38]C. Yamabe, S. J. Buckman, and A. V. Phelps, "Measurement of free-free emission from low-energy-electron collisions with Ar," **27**, 1345–1352.
[39]A. V. Phelps, "The application of scattering cross sections to ion flux models in discharge sheaths," **76**, 747–753.
[40]See `https://us.lxcat.net/contributors/#d19`.
[41]See `https://github.com/PhysicsPlasma/iPM1D2019`.
[42]S. Yu, H. Wu, J. Xu, Y. Wang, J. Gao, Z. Wang, W. Jiang, and Y. Zhang, "A generalized external circuit model for electrostatic particle-in-cell simulations," Computer Physics Communications **282**, 108468 (2023).
[43]J. Gao, S. Yu, H. Wu, Y. Wang, Z. Wang, Y. Pan, W. Jiang, and Y. Zhang, "Self-consistent simulation of the impedance matching network for single frequency capacitively coupled plasma," Journal of Physics D: Applied Physics **55**, 165201 (2022).
[44]S. Yu, H. Wu, S. Yang, L. Wang, Z. Chen, Z. Wang, W. Jiang, J. Schulze, and Y. Zhang, "Kinetic simulations of capacitively coupled plasmas driven by tailored voltage waveforms with multi-frequency matching," Plasma Sources Science and Technology **33**, 075003 (2024).
[45]Y.-l. Shen, Y.-q. Tu, L.-j. Chen, and T.-a. Shen, "Phase difference estimation method based on data extension and hilbert transform," Measurement Science and Technology **26**, 095003 (2015).
[46]M. Rosenblum, A. Pikovsky, A. A. Kühn, and J. L. Busch, "Real-time estimation of phase and amplitude with application to neural data," Scientific Reports **11**, 18037 (2021).

[47] P. V. Nikitin, K. V. S. Rao, S. F. Lam, V. Pillai, R. Martinez, and H. Heinrich, "Power reflection coefficient analysis for complex impedances in rfid tag design," IEEE Transactions on Microwave Theory and Techniques **53**, 2721–2725 (2005).

[48] R. J. Sprungle and E. F. Kuester, "A comparison of two methods for defining the reflection coefficient," in *2023 United States National Committee of URSI National Radio Science Meeting (USNC-URSI NRSM)* (IEEE, Boulder, CO, USA, 2023) pp. 92–93.

[49] F. Yan, Q. Zhuang, M. Yang, K. Kang, Z. Xiong, and C. Yuan, "Broadband polarization-adjustable antenna realized by waveguide circular polarizers," Review of Scientific Instruments **95**, 104710 (2024).

[50] U. Rusdiana, I. Ernawati, N. Falih, and A. Arista, "Comparison of distance metrics on fuzzy c-means algorithm through customer segmentation," in *2021 International Conference on Informatics, Multimedia, Cyber and Information System (ICIMCIS)* (IEEE, Jakarta, Indonesia, 2021) pp. 307–311.

[51] R. Storn and K. Price, "Differential evolution: A simple and efficient heuristic for global optimization over continuous spaces," Journal of Global Optimization **11**, 341–359 (1997).

[52] I. Ahmadianfar, O. Bozorg-Haddad, and X. Chu, "Gradient-based optimizer: A new metaheuristic optimization algorithm," Information Sciences **540**, 131–159 (2020).

[53] S. K. Mishra and B. Ram, *Introduction to Unconstrained Optimization with R* (Springer Singapore, Singapore, 2019).

[54] M. Ye, H. Zhou, H. Yang, B. Hu, and X. Wang, "Multi-strategy improved dung beetle optimization algorithm and its applications," Biomimetics **9**, 291 (2024).

[55] Y. Li, K. Sun, Q. Yao, and L. Wang, "A dual-optimization wind speed forecasting model based on deep learning and improved dung beetle optimization algorithm," Energy **286**, 129604 (2024).

[56] J. Xue and B. Shen, "Dung beetle optimizer: A new meta-heuristic algorithm for global optimization," The Journal of Supercomputing **79**, 7305–7336 (2023).

[57] M. Vass, S. Wilczek, T. Lafleur, R. P. Brinkmann, Z. Donkó, and J. Schulze, "Observation of dominant ohmic electron power absorption in capacitively coupled radio frequency argon discharges at low pressure," Plasma Sources Science and Technology **29**, 085014 (2020).

[58] S. Simha, S. Sharma, A. Khrabrov, I. Kaganovich, J. Poggie, and S. Macheret, "Particle-in-cell simulation of a 50 mtorr capacitively coupled argon discharge over a range of frequencies," (2023), 2306.05386.

[59] X.-M. Zhu, W.-C. Chen, S. Zhang, Z.-G. Guo, D.-W. Hu, and Y.-K. Pu, "Electron density and ion energy dependence on driving frequency in capacitively coupled argon plasmas," Journal of Physics D: Applied Physics **40**, 7019–7023 (2007).

[60] S. Yang, W. Zhang, J. Shen, H. Liu, C. Tang, Y. Xu, J. Cheng, J. Shao, J. Xiong, X. Wang, H. Liu, J. Huang, X. Zhang, H. Lan, and Y. Li, "Influence of radio frequency wave driving frequency on capacitively coupled plasma discharge," AIP Advances **14**, 065104 (2024).

[61] S. J. You, H. C. Kim, C. W. Chung, H. Y. Chang, and J. K. Lee, "Mode transition for power dissipation induced by driving frequency in capacitively coupled plasma," Journal of Applied Physics **94**, 7422–7426 (2003).

[62] E. Semmler, P. Awakowicz, and A. von Keudell, "Heating of a dual frequency capacitively coupled plasma via the plasma series resonance," Plasma Sources Science and Technology **16**, 839–848 (2007).

[63] S. Wilczek, J. Trieschmann, J. Schulze, E. Schuengel, R. P. Brinkmann, A. Derzsi, I. Korolov, Z. Donkó, and T. Mussenbrock, "The effect of the driving frequency on the confinement of beam electrons and plasma density in low-pressure capacitive discharges," Plasma Sources Science and Technology **24**, 024002 (2015).

[64] S. Sharma, N. Sirse, and M. M. Turner, "High frequency sheath modulation and higher harmonic generation in a low pressure very high frequency capacitively coupled plasma excited by sawtooth waveform," Plasma Sources Science and Technology **29**, 114001 (2020).

[65] D. Gahan and M. B. Hopkins, "Collisionless electron power absorption in capacitive radio-frequency plasma sheaths," Journal of Applied Physics **100**, 043304 (2006).